Research Square

Preprints are preliminary reports that have not undergone peer review.
They should not be considered conclusive, used to inform clinical practice,
or referenced by the media as validated information.

Adaptive constrained first-arrival tomography driven by uphole velocity priors for complex near-surface imaging

Huo Yuanyuan
North China University of Water Resources and Electric Power
Yang Rui
yangr@mail.cgs.gov.cn
Qingdao Institute of Marine Geology https://orcid.org/0009-0004-4889-846X
Qi Hui
North China University of Water Resources and Electric Power
Li Xin
Sinopec: China Petrochemical Corporation

Research Article

Keywords: Constrained tomography, Uphole survey priors, Complex near-surface, Loess Plateau, Long-wavelength statics

Posted Date: September 1st, 2026

DOI: https://doi.org/10.21203/rs.3.rs-10677710/v1

License: This work is licensed under a Creative Commons Attribution 4.0 International License.
Read Full License

Adaptive constrained first-arrival tomography driven by uphole velocity priors for complex near-surface imaging

Huo Yuanyuan[1] ， Yang Rui[2,3*] ， Qi Hui[1] ， Li Xin[4]

1. North China University of Water Resource and Electric Power，Zhengzhou，450000，China；huoyuanyuan@ncwu.edu.cn

2. The Key Laboratory of Gas Hydrate, Ministry of Natural Resources, Qingdao Institute of Marine Geology, Qingdao 266237, China; yangr@mail.cgs.gov.cn

3. Laboratory for Marine Mineral Resources, Qingdao National Laboratory for Marine Science and Technology, Qingdao 266237, China;

4. Exploration and Development Research Institute of North China Oil and Gas Company, SINOPEC, Zhengzhou，450000, China

Abstract

High-precision seismic imaging of shallow thin interbedded reservoirs is critical for continental lithologic hydrocarbon exploration. Complex near-surface environments on China's Loess Plateau bring severe challenges: laterally variable low-velocity zones (LVZs), rugged topography and restricted acquisition layouts create extremely sparse shallow ray coverage (effective fold < 10). Such sparsity invalidates the foundational hypothesis of traditional refraction statics and triggers large null spaces in the Jacobian matrix as well as Hessian singularities in conventional traveltime tomography, which produce anomalous LVZ stretching artifacts and severe static errors. To relieve the non-uniqueness of traveltime inversion, we propose an adaptively constrained first-arrival tomography constrained by uphole velocity priors. Measured absolute uphole velocities are transformed into slowness and embedded into the standard Tikhonov objective function. To realize stable fusion of prior constraints and seismic traveltime data, a novel horizontally–vertically decoupled Gaussian kernel is constructed for regularization weight matrix **W**, which effectively eliminates bullseye artifacts common in traditional well-constrained inversions. Sparse synthetic experiments prove that the proposed method mitigates ill-posed artifacts, cutting the global velocity root-mean-square error (RMSE) by 65.6% (from 15.4 m/s to 5.3 m/s) relative to unconstrained tomography. For the 3D seismic dataset of the Weibei Oilfield, the optimal Gaussian influence radius of 500 m is calibrated by maximizing stacked root-mean-square (RMS) amplitude within an 80 ms time window, paired with a 30% normal moveout (NMO) stretch muting threshold. Blind-well verification achieves a velocity prediction error of merely 12 m/s. This method generates reliable near-surface velocity models and accurate static corrections, supporting high-fidelity seismic imaging across complex near-surface areas.

Keywords Constrained tomography; Uphole survey priors; Complex near-surface; Loess Plateau; Long-wavelength statics

Introduction

High-precision seismic imaging of shallow thin interbeds is critical for exploring continental lithologic hydrocarbon reservoirs like the Weibei Oilfield in the Ordos Basin. The fidelity of target formation imaging and the effectiveness of static corrections rely entirely on the accuracy of the near-surface velocity model. In the loess tableland regions of the western Loess Plateau, near-surface velocity modeling faces severe challenges driven by extreme topographic relief, abrupt lateral variations in the weathered layer, and strong velocity heterogeneity (Li et al. 2004; Hu et al. 2010; Yu et al. 2016). These geological complexities are exacerbated by restricted acquisition layouts around nature reserves and abandoned mines, leading to ultra-low effective data folds and extensive ray illumination blind zones (Liu et al. 1995; Zhu et al. 2024). Overcoming these ultra-low fold and sparse well constraints to build accurate near-surface models and suppress long-wavelength static correction errors remains a critical, ongoing challenge in onshore seismic exploration (Chang et al. 2002).

Extensive research has focused on static correction and velocity modeling for complex near-surface media. Traditional refraction statics rely on the assumption of horizontally layered media, retrieving parameters for low-velocity and subweathered zones via intercept-time and delay-time methods. While effective in gently rolling terrains with stable strata (Xiao et al. 2019), these techniques fundamentally fail in the gully-dissected loess tablelands. Intense topographic relief and variable stratigraphic attitudes severely violate the horizontal-layer assumption, degrading the accuracy of refraction tracking and parameter inversion, and thereby failing to effectively resolve long-wavelength static corrections (Ju and Yu 2017; Dai et al. 2020).

To accommodate rugged topography and heterogeneous media, first-arrival traveltime tomography has emerged as the mainstream near-surface modeling technique. By establishing a linear relationship between traveltime residuals and slowness perturbations based on ray theory, this method retrieves the near-surface velocity field via regularized iterative inversion, theoretically adapting to arbitrarily complex architectures (Ivansson et al. 1986; Zhang and Wang 2024). However, the inversion accuracy heavily depends on ray coverage density and angular diversity. Under ultra-low-fold acquisition conditions, seismic rays within the shallow 0–200 m interval propagate nearly vertically. This severe lack of crossing paths creates an extensive null space in the Jacobian matrix and severe singularity in the local approximate Hessian matrix (Pratt and Chapman 1992; Bregman et al. 1989; Morozov 2004). Consequently, inversion artifacts—such as the anomalous stretching of low-velocity zones and blurred velocity boundaries—frequently degrade the results (Bube and Meadows 1999). To maintain numerical stability, standard workflows mitigate this ill-posedness by heavily weighting smoothing regularization; however, this fundamentally sacrifices model resolution and yields excessively smoothed near-surface velocity interfaces (Portniaguine and Zhdanov 1999).

Spatial weighting constraints utilizing Gaussian kernel functions have increasingly been adopted in tomographic inversion. By leveraging distance-dependent attenuation, these functions control the spatial influence of prior information to smoothly transition from local constraints to the global velocity field (Goudswaard et al. 1998; Bakulin et al. 2009). However, most existing applications default to isotropic Gaussian kernels with uniform horizontal and vertical attenuation radii (Charles et al. 2006). This isotropic assumption fails in sedimentary near-surface media, particularly within the thin interbedded structures of loess tablelands, where vertical velocity gradients vastly exceed lateral variations and manifest as sharp vertical boundaries. Consequently, isotropic weighting introduces a fundamental numerical dilemma: rapid attenuation provokes

bullseye artifacts, while slow attenuation causes unphysical vertical cross-layer smoothing (Jordi et al. 2018). This makes it impossible to simultaneously preserve sharp vertical interfaces and gentle lateral variations. Furthermore, while existing research on loess tablelands has predominantly focused on acquisition geometry optimization, first-break picking enhancements, or standalone interpolation strategies, studies addressing regularization constraint mechanisms under extreme sparse-data conditions (effective fold < 10, well spacing > 1000 m) remain critically insufficient (Rao 2007). A comprehensive theoretical framework encompassing anisotropic kernel design, quantitative parameter calibration, and inversion convergence mechanisms is currently lacking.

To address these challenges, this study proposes an adaptively constrained first-arrival tomography method driven by uphole velocity priors. Compared with traditional well-constrained approaches, the core academic and technical contributions of this work are threefold. First, breaking from the conventional isotropic framework, we design a horizontally and vertically decoupled Gaussian kernel weight matrix **W** tailored to the sedimentary anisotropy of near-surface media (Li et al. 2021). This structural decoupling preserves sharp vertical velocity boundaries while enabling a smooth transition of lateral constraints, fundamentally suppressing bullseye artifacts and over-smoothing at the kernel design level. Second, absolute slowness data from uphole surveys are incorporated into the standard Tikhonov objective function as adaptive regularization terms (Trinks et al. 2005). By adopting trace-ratio energy normalization to balance the gradient energy between the prior constraint and data fitting terms, we successfully condition the Hessian matrix within ill-posed regions, mathematically resolving null-space singularities under ultra-low-fold conditions. Third, we propose a quantitative parameter calibration criterion based on maximizing the stacked RMS amplitude of target formations (Ronen and Claerbout 1985). Combined with independent blind-well verification using a representative well in a highly heterogeneous zone, this establishes a data-driven, closed-loop parameter optimization framework that operates without a true subsurface model (Dahl 1989). This provides a robust solution to the longstanding engineering problem of determining optimal regularization parameters in field production.

In this paper, we first analyze the ill-posed nature of conventional tomography and derive the mathematical formulation of the adaptively constrained objective function, including the explicit construction scheme for the weight matrix **W**. We then investigate the associated inversion gradients and convergence mechanisms. To quantitatively verify the precision and stability of the proposed method, we construct synthetic geological models that mirror the stratigraphic features of actual loess tablelands, conducting multi-strategy comparisons and single-well robustness tests under extreme sparse-data conditions. Finally, we apply the workflow to a 3D field seismic dataset from the Weibei Oilfield. Comprehensive blind-well verifications and imaging comparisons demonstrate the method's industrial applicability, offering a robust technical framework for high-precision static corrections in loess tablelands and similar complex near-surface regimes.

Theory and methodology

Limitations of conventional tomography and mathematical reformulation

Traditional ray-based first-arrival traveltime tomography is a highly non-linear optimization problem. The conventional inversion scheme minimizes data misfit and applies model-space smoothing regularization to mitigate non-uniqueness, typically following the Tikhonov regularization framework (Tikhonov and Arsenin 1977). The standard objective function is expressed as:

$$E(\mathbf{m}) = \frac{1}{2}(\mathbf{d} - \mathbf{T}(\mathbf{m}))^{\mathrm{T}}\mathbf{C}_{\boldsymbol{d}}^{-1}(\mathbf{d} - \mathbf{T}(\mathbf{m})) + \frac{1}{2}\lambda\|\mathbf{Lm}\|_2^2 \quad (1)$$

where **m** is the model parameter vector, strictly defined as slowness (the reciprocal of velocity) to enhance linearity; $\mathbf{C}_d^{-1}$ is the inverse data covariance matrix accounting for traveltime picking uncertainties; **d** and **T(m)** denote the observed and theoretical forward-modeled first-arrival traveltime vectors, respectively; λ is the regularization parameter balancing data misfit and smoothing constraints; and **L** is the Laplacian operator matrix penalizing variations between adjacent computational grids.

While effective under standard, high-density geometries, this objective function struggles in complex near-surface environments with severe topography and ultra-low fold coverage. In regions like the Loess Plateau, seismic rays penetrate nearly vertically, creating a critical deficit of crossing raypaths in the shallow 0-200 m interval. This deficient illumination geometry renders the local inversion system severely under-determined.

Mathematically, the partial derivatives of traveltime residuals nearly vanish in these ray-blind zones, creating a massive null space within the Jacobian matrix. Consequently, during Gauss-Newton optimization, the approximate Hessian matrix $\mathbf{G}^{\mathrm{T}}\mathbf{G}$ exhibits extreme local singularity (Jin et al. 1992). To maintain numerical stability, conventional workflows forcibly increase the smoothing weight λ. However, this severely compromises resolution, inducing anomalous stretching or over-smoothing artifacts in the LVZ that blur true velocity interfaces and cause drastic errors in long-wavelength static calculations.

To eliminate the local Jacobian singularities caused by ultra-low fold coverage and resolve the severe non-uniqueness of pure traveltime inversion, deterministic physical constraints must be introduced to strictly anchor the solution's null space. Therefore, we incorporate high-precision absolute slowness data from local uphole surveys as prior information. This allows us to reformulate the conventional tomographic objective function by embedding a novel adaptive constraint regularization term (Soni et al. 2019):

$$E(\mathbf{m}) = \frac{1}{2}(\mathbf{d} - \mathbf{T}(\mathbf{m}))^{\mathrm{T}}\mathbf{C}_{\boldsymbol{d}}^{-1}(\mathbf{d} - \mathbf{T}(\mathbf{m})) + \frac{1}{2}\lambda\|\mathbf{Lm}\|_2^2 + \frac{1}{2}\gamma\left\|\mathbf{W}(\mathbf{m} - \mathbf{m}_{prior})\right\|_2^2 \quad (2)$$

Here, the third term represents an adaptive constraint regularization based on prior uphole data. In this formulation, $\mathbf{m}_{prior}$ is the prior slowness model vector interpolated from absolute uphole velocity measurements; γ is a hyperparameter controlling the overall strength of the prior constraint; and **W** is a novel spatially adaptive kernel weighting matrix (detailed subsequently). Specifically, **W** is engineered to precisely dictate the effective 3D spatial footprint and decay gradient of these prior constraints.

The reformulated objective function offers significant physical and mathematical advantages. In regions with dense ray coverage, the data-misfit term dominates, ensuring the high-fidelity reconstruction of fine-scale structures. Conversely, in ray-blind zones and near uphole locations, the prior constraint term strongly intervenes, anchoring the inversion to absolute physical ground truths and preventing numerical divergence. Mathematically, this mechanism injects strictly positive values into localized segments of the main diagonal of the ill-conditioned approximate Hessian matrix. Together with global smoothing, this improves the overall condition number of the normal equations. Physically, it establishes a robust boundary constraint for ultra-low fold near-surface modeling, effectively preventing velocity stretching and "bullseye" artifacts at their source.

Design of the spatially adaptive constraint weight matrix

Within the reconstructed objective function, the design of the weighting matrix **W** is crucial for accurately integrating prior data. Conventional constrained tomographic frameworks typically rely on inverse distance weighting (IDW) or isotropic Gaussian decay (Shepard 1968). However, complex near-surface media like the Loess Plateau exhibit strong macroscopic anisotropy. Governed by natural deposition and compaction, vertical velocity gradients significantly exceed lateral variations, especially in shallow, thin-interbedded zones with sharp vertical velocity interfaces.

Consequently, applying traditional isotropic weights creates a numerical dilemma: a rapid spatial decay generates unphysical "bullseye" artifacts near wells, whereas a slow decay causes excessive vertical cross-layer smoothing that obliterates the true boundaries of the LVZ.

To account for this anisotropic correlation, we replace the conventional isotropic assumption with a separable Gaussian kernel function based on physical space decoupling. For the i-th node in the inversion grid and the k-th depth sampling point of the uphole, the constraint weight $W_{i,k}$ is defined as Rawlinson and Sambridge (2005):

$$w_{i,k} = \exp\left(-\left[\frac{(x_i - X_{well})^2 + (y_i - Y_{well})^2}{2\sigma_h^2} + \frac{(z_i - z_k)^2}{2\sigma_v^2}\right]\right) \tag{3}$$

where $(x_i,\ y_i,\ z_i)$ are the 3D coordinates of the i-th inversion grid node; $(X_{well},\ Y_{well})$ are the horizontal coordinates of the uphole; z_k is the depth of the k-th uphole sampling point; and σ_h and σ_v are the horizontal and vertical Gaussian decay radii, respectively, which independently control the spatial decay rate of the prior information. Given the high vertical sampling density (1–2 m) of the uphole data, we fix σ_v to a constant 5 m to match the vertical grid spacing (Δz). This prevents unphysical smoothing across sharp vertical velocity boundaries. Consequently, the hyperparameter search is simplified to a 1D optimization problem focused solely on σ_h, the core spatial parameter governing lateral constraint propagation, which is dynamically optimized in subsequent sections.

Numerically, the calculated weights $W_{i,k}$ are assembled into a sparse diagonal matrix $\mathbf{W}$=diag($w_1, w_2, \ldots, w_N$), where N is the total number of 3D grid nodes. To optimize computational efficiency and reduce memory demands during large-scale inversion, we apply a spatial truncation threshold, assigning non-zero weights exclusively to nodes within the effective influence radius (defined by the 3σ confidence interval). Ultimately, this spatially decoupled weighting mechanism provides essential mathematical regularization for ultra-shallow ray-blind zones while preserving the geological plausibility and kinematic fidelity of the inversion results.

Gradient analysis and convergence mechanism of the objective function

Because minimizing the reformulated objective function is a highly nonlinear problem, we solve it using a Gauss-Newton iterative scheme, which balances convergence efficiency and numerical stability for large-scale sparse systems (Nocedal and Wright 2006). By taking the first-order partial derivative of the constrained objective function with respect to the slowness vector **m**, we derive the global gradient vector **g** for the current iteration：

$$\mathbf{g} = \nabla E(\mathbf{m}) = -\mathbf{G}^{\mathrm{T}}\mathbf{C}_{\boldsymbol{d}}^{-\mathbf{1}}(\mathbf{d} - \mathbf{T}(\mathbf{m})) + \lambda\mathbf{L}^{\mathrm{T}}\mathbf{L}\mathbf{m} + \gamma\mathbf{W}^{\mathrm{T}}\mathbf{W}(\mathbf{m} - \mathbf{m}_{prior}) \tag{4}$$

where **G** is the Jacobian (or sensitivity) matrix containing the current raypath geometry. Its elements represent the first-order partial derivatives of traveltimes with respect to the model parameters, reflecting the linear response to minute model

perturbations. By evaluating the second-order derivatives and neglecting higher-order terms caused by nonlinear ray bending (the standard Gauss-Newton approximation), the updated approximate Hessian matrix, **H**, is formulated as:

$$\mathbf{H} \approx \mathbf{G}^{\mathrm{T}}\mathbf{C}_{d}^{-1}\mathbf{G} + \lambda\mathbf{L}^{\mathrm{T}}\mathbf{L} + \gamma\mathbf{W}^{\mathrm{T}}\mathbf{W} \tag{5}$$

In conventional traveltime tomography, ultra-low shallow coverage creates ray-blind zones where the eigenvalues of the data-driven $\mathbf{G}^{\mathrm{T}}\mathbf{G}$ matrix approach zero, rendering the approximate Hessian severely ill-conditioned. Our proposed adaptive weighting mitigates this via the $\gamma\mathbf{W}^{\mathrm{T}}\mathbf{W}$ term, a positive semi-definite diagonal matrix that localizes constraint energy strictly within the effective radius of the uphole survey data.

Although this spatially truncated matrix contains zero elements in the unconstrained far-field, the global smoothing term ($\lambda\mathbf{L}^{\mathrm{T}}\mathbf{L}$) guarantees the positive-definiteness and numerical stability of the complete Hessian. Combined, these mechanisms ensure a strictly well-conditioned system for gradient-based optimization.

At each iteration, computing the model update $\Delta\mathbf{m}$ requires solving a large-scale, sparse system of normal equations ($\mathbf{H}\Delta\mathbf{m}=-\mathbf{g}$). Because the prior constraints significantly improve the condition number of this symmetric positive-definite (SPD) matrix, we efficiently solve the system using the Conjugate Gradient (CG) method (Hestenes and Stiefel 1952).

This spatially decoupled regularization synergizes with the CG algorithm to suppress singularities arising from the Jacobian's null space. Consequently, it ensures numerical robustness, circumvents the divergence and local minima traps common in ultra-low fold scenarios, and guarantees smooth convergence toward a geologically meaningful optimum.

Energy normalization and optimization principles of global constraint weights

Integrating prior constraints into the tomographic objective function introduces inherent disparities in physical dimensions and energy scales among the traveltime data misfit (time), spatial smoothing operators (dimensionless or inverse-length), and prior constraints (slowness). To automatically balance the gradient contributions between the data misfit and the uphole survey constraints, we introduce a dimensional scaling hyperparameter, γ, following the trace-ratio energy normalization principle (Grote et al. 2017). This parameter dynamically matches the energy magnitude of the spatially decoupled Gaussian weights to the primary objective function, calculated via the trace ratio of their respective Hessian approximations:

$$\gamma = \alpha \cdot \frac{\mathrm{Tr}(\mathbf{G}^{\mathrm{T}}\mathbf{C}_{d}^{-1}\mathbf{G})}{\mathrm{Tr}(\mathbf{W}^{\mathrm{T}}\mathbf{W})} \tag{6}$$

where Tr denotes the trace operator, which evaluates the matrix's global energy distribution; **W** is the spatial weighting matrix; and α is a dimensionless scalar that regulates the relative intensity of the prior constraints. By calibrating the data misfit and prior constraint gradients to an identical energy scale, this normalization ensures robust convergence during early nonlinear iterations and preserves the numerical well-posedness of the normal equations.

With energy balance and stable gradient updates established, the accurate calibration of the spatial Gaussian influence radius (σ_h) remains the primary challenge dictating the fidelity of prior constraints. In complex near-surface scenarios with ultra-low coverage, jointly optimizing hyperparameters and model parameters is numerically demanding.

While global optimization strategies (such as Genetic Algorithms) are frequently used in highly nonlinear problems like

surface-wave full-waveform inversion to avoid local minima (Huo et al. 2024), their immense computational overhead makes them impractical for industrial-scale 3D traveltime tomography, which typically involves millions of grid nodes.

To replace subjective trial-and-error, we propose an efficient, data-driven optimization criterion. Based on the seismological principle that accurate static corrections enhance the lateral coherence of subsurface reflections, we adopt the RMS amplitude within the stacking time window of key target horizons as the quantitative metric (Linari 2004). This establishes a geologically meaningful objective function:

$$f(\sigma_h) = \mathrm{RMS}_{target}(\sigma_h) \longrightarrow max \tag{7}$$

In practice, this alternating optimization strategy reduces the strongly coupled 2D nonlinear problem into stable 1D search processes. First, across a predefined array of candidate σ_h values, we execute a series of independent tomographic inversions using the CG algorithm. Subsequently, the statically corrected seismic data are stacked, and the RMS energy within the time window of the target horizon (e.g., the Chang 3 reservoir) is extracted.

By identifying the global peak of this 1D RMS energy curve, the optimal constraint influence radius is determined objectively, bypassing the need for computationally expensive global optimization algorithms. Ultimately, this data-driven criterion significantly enhances computational efficiency and establishes a highly reproducible workflow for static corrections in ultra-low fold environments.

Synergy and decoupling mechanism between prior slowness gradient and spatial smoothing operators

To overcome the ill-conditioning of the Jacobian matrix, conventional first-arrival traveltime tomography typically incorporates a global first- or second-order differential smoothing operator, **L**, as a regularization constraint (Simmons et al. 2012). However, conventional smoothing operators inherently penalize slowness differences between adjacent spatial grids. This inevitable homogenization severely blurs the true vertical and horizontal slowness gradients of complex near-surface structures.

By introducing uphole survey prior constraints in our proposed method, the objective function integrates both the global smoothing operator term and the adaptive prior constraint term. Rather than mathematically competing, these two regularization terms achieve adaptive spatial decoupling and a dynamic trade-off via the spatial Gaussian weighting matrix, **W**:

(1) Near-Well Control Zone (Gradient Retention Dominant): In the immediate vicinity of an uphole survey, as the spatial distance $d_i \to 0$, the corresponding diagonal element of the adaptive Gaussian weighting matrix approaches unity ($\mathbf{W}_{ii} \to 1$). Consequently, the mathematical weight of the prior constraint significantly dominates over the global smoothing operator (i.e., $\gamma \mathbf{W}_{ii}^2 \gg \lambda(\mathbf{L}^{\mathrm{T}}\mathbf{L})_{ii}$). During the optimization iterations, the objective function in this region strongly prioritizes fitting the prior slowness baseline provided by the uphole survey, along with its inherent sharp vertical gradients. The smearing effect of the global smoothing operator is effectively suppressed here, guaranteeing high fidelity at known data points and preserving sharp structural boundaries.

(2) Far-Well Unconstrained Zone (Dominated by Smoothing and Spatial Coupling): As the spatial distance from the control well increases (i.e., $d_i \gg \sigma$), the Gaussian weighting decays exponentially. At this distance, the direct enforcement of the prior constraint fades, and the objective function reduces to a form akin to conventional smoothing tomography. However, a fundamental distinction exists in the underlying mathematical mechanism: under the proposed synergistic framework, the global smoothing operator functions not merely to suppress high-frequency noise, but crucially, it acts as a "transmission mechanism" for spatial coupling. Facilitated by the off-diagonal elements of the smoothing matrix, the highly stable solutions near the wells effectively serve as boundary conditions that extrapolate outward to the unconstrained peripheries. This spatial coupling eliminates the "global drift" induced by the null space of the Jacobian matrix, ensuring that numerical updates in the far-field grids are no longer isolated, ill-posed optimizations. Instead, they operate as a well-posed extension anchored to a reliable near-field structural skeleton, thereby guaranteeing the robustness of the nonlinear solution within ray-blind zones.

In summary, mediated by the adaptive weighting matrix **W**, the proposed algorithm establishes a robust spatial synergy: high-fidelity well-log constraints anchor true gradients near the boreholes, transition zones bridge variations smoothly, and unconstrained far-field regions are stabilized by conventional smoothing. This innovative framework fundamentally overcomes the over-smoothing and gradient degradation that indiscriminate global regularization typically imposes on true geological structures.

Synthetic data test

Synthetic model building and acquisition geometry configuration

To evaluate the proposed algorithm's robustness and accuracy under ultra-low fold scenarios and complex loess tableland conditions, we built a 2D acoustic velocity model that closely mimics realistic geological structures. Discretized with a grid spacing of $\Delta x=\Delta z=5$ m, the model extends 5000 m horizontally and 1200 m vertically. It integrates the following key geological features:

(a) Topography and Geomorphology: The model captures the severely eroded, ravine-dissected terrain characteristic of the loess tableland. It incorporates three to four deeply incised valleys with a maximum topographic relief of 150–250 m, faithfully replicating the rugged surface conditions.

(b) Near-Surface LVZ Structure:

- Uppermost Layer (Surficial Loess): Seismic velocities range from 200 to 500 m/s. This layer exhibits strong lateral heterogeneity, with thicknesses varying drastically between 20 and 200 m.
- Second Layer (Underlying Clay): Velocities range from 600 to 1000 m/s, with thicknesses similarly demonstrating significant lateral variation between 20 and 200 m.

(c) High-Velocity Bedrock and Velocity Gradients:

- Bedrock Top Interface (Velocity Discontinuity): A sharp velocity contrast separates the unconsolidated overburden from the underlying bedrock, where the velocity abruptly increases to 2500 m/s.

- Internal Bedrock Features: With increasing depth, the bedrock velocity exhibits a continuous positive vertical gradient, reaching a maximum of 3600 m/s at the base of the model.

To rigorously simulate the ultra-low fold conditions typical of legacy seismic data or irregular field surveys, the acquisition geometry is configured with a sparse shot interval of 200 m and a receiver interval of 20 m. All first-arrival traveltimes are computed using a high-order finite-difference fast marching method (FMM) to solve the eikonal equation.

Under the sparse acquisition geometry (effective fold < 10), shallow raypath distribution exhibits severe spatial heterogeneity. Statistical analysis of forward-modeled raypaths indicates that within the shallowest depth interval (0-200 m), the average ray hit count is only 1.8 per grid node, with some nodes in the core LVZ registering zero hits (forming ray shadow zones). Furthermore, because transmitted rays emerge predominantly in a near-vertical direction, the density of crossing ray pairs approaches zero. This adverse illumination causes the condition number of the normal equation matrix ($\mathbf{G}^T\mathbf{G}$) to surge to 1.4×10^6, creating a vast null space. This ill-conditioning is the primary physical cause of the severe "bulls-eye" artifacts and velocity smearing observed in conventional traveltime tomography.

Tomographic inversion results and quantitative error analysis

To rigorously evaluate the vertical resolution and fidelity of the inverted model at a finer local scale, a 1D vertical velocity profile was extracted at lateral coordinate X=2500 m (Fig. 1). A detailed analysis of this profile reveals the following:

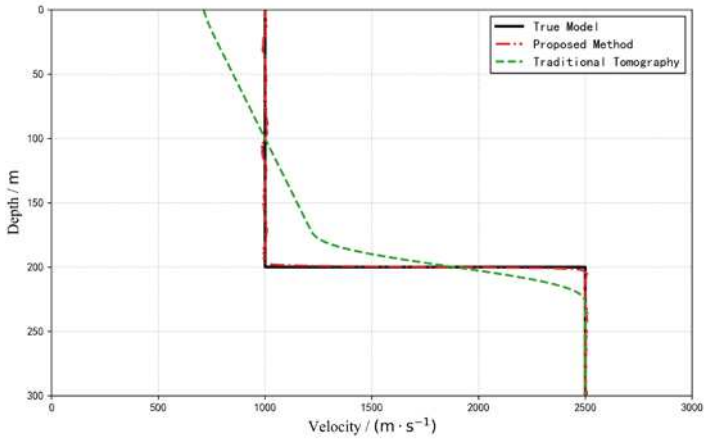


Fig. 1 Comparison of vertical velocity profiles versus depth

A detailed analysis of Fig. 1 reveals the following:

1. Within the 0–200 m low-velocity zone, conventional methods suffer from ray shadow-zone limitations, yielding an erroneous pseudo-linear velocity increase from 700 to 1300 m/s. In contrast, the constrained inversion profile proposed in this study closely matches the true velocity, with the absolute error strictly contained within ±15 m/s.

2. At the bedrock interface (at a depth of 200 m), the true model exhibits a discrete velocity jump from 1000 to 2500 m/s. Due to inherent over-smoothing, conventional tomography blurs this boundary into a broad transition zone spanning nearly 60 m. In contrast, the proposed method precisely resolves this abrupt velocity contrast and accurately pinpoints its depth without artificial smearing.

These comprehensive quantitative results conclusively demonstrate that in severely ill-posed ray shadow zones, incorporating deterministic prior constraints from uphole survey is essential for preserving the structural fidelity of shallow, thinly interbedded velocity models.

Furthermore, to rigorously and quantitatively assess the algorithm's inversion accuracy, this study adopts the RMSE across the entire near-surface grid as the primary evaluation metric:

$$\mathrm{RMSE} = \sqrt{\frac{1}{M}\sum_{j=1}^{M}(v_j^{inv} - v_j^{true})^2} \tag{8}$$

where M denotes the total number of grid nodes; v_j^{inv} represents the inverted velocity (obtained by taking the reciprocal of the inverted slowness) at the j-th node, and v_j^{true} indicates the corresponding true velocity. Quantitative results show that the global RMSE of the conventional smoothing tomography model is 15.4 m/s. In contrast, the proposed adaptive constrained tomography model reduces the global RMSE to 5.3 m/s, achieving a substantial 65.6% reduction in the overall prediction error.

Additionally, Fig.2 compares the objective function convergence curves of both methods. As observed, conventional tomography suffers from pronounced gradient stagnation, becoming trapped in a local minimum after the sixth iteration.

In contrast, by enhancing the positive-definiteness of the local diagonal elements in the Hessian matrix, the proposed method achieves a rapid reduction in the objective function during the first five iterations. Between iterations 6 and 10, the convergence curve exhibits transient numerical oscillations caused by the intense lateral velocity gradients of the loess tableland model. These fluctuations reflect the optimization algorithm's navigation through complex, highly nonlinear valleys in the objective function landscape. Ultimately, beyond iteration 12, the algorithm successfully escapes the stagnation plateau and asymptotically stabilizes. This behavior not only highlights a substantial improvement in convergence efficiency but also demonstrates the method's numerical robustness under adverse data conditions.

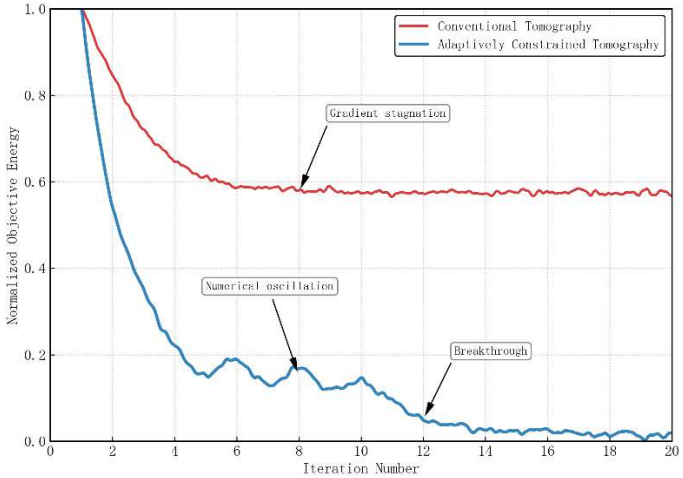


Fig.2 Convergence curves of the normalized objective function versus iteration number for the two methods

Performance comparison of alternative prior strategies and validation of the gaussian decay mechanism

To quantitatively demonstrate the advantages and necessity of the proposed spatial Gaussian decay weighting mechanism over standard constraint strategies, comparative tests involving four distinct constraint approaches were conducted on the synthetic model:

- Strategy A (Unconstrained conventional smoothing tomography): Yields a global RMSE of 15.4 m/s. As previously discussed, this method fails to accurately resolve structures within the ray shadow zones.
- Strategy B (Direct hard constraint): Slowness values at the uphole survey nodes are strictly fixed to the measured ground truth and excluded from iterative updates, yielding an RMSE of 12.1 m/s. However, the extreme gradient variations between adjacent grid nodes induce severe spatial discontinuities and unnatural "bulls-eye" artifacts around the well locations.
- Strategy C (Constant-weight soft constraint): Uniform prior constraint weights are applied to all nodes across the entire domain (i.e., $w_i \equiv W_{max}$). While this approach yields an RMSE of 9.8 m/s and eliminates local bulls-eye artifacts, it forcibly biases grid nodes far from the wellbores toward a smoothly interpolated prior model. Consequently, it severely suppresses the data-driven resolving power of the seismic traveltimes.
- Strategy D (Proposed Gaussian adaptive constraint): By explicitly controlling the spatial decay of the constraint intensity based on physical distance, the global RMSE is reduced to an optimal 5.3 m/s, demonstrating robust capability in confining the inversion solution space. This strategy not only utilizes uphole data to firmly anchor the LVZ bottom boundary in the shallowest layers, but also seamlessly returns update dominance to the seismic data in deeper zones and intermediate-to-far offsets, successfully preserving high-frequency geological details.

These quantitative comparative experiments demonstrate that in complex near-surface environments with strong lateral variations, incorporating the Gaussian decay mechanism is an essential mathematical framework. It optimally balances local prior constraints with global data-driven updates, effectively mitigating both model overfitting and underfitting.

Sparsity sensitivity analysis and single-well robustness testing

In real-world seismic surveys, challenging topography and strict budgetary constraints often limit prior data acquisition to extremely sparse, or even single, uphole survey datasets within a survey area. To rigorously evaluate the operational limits and numerical robustness of the proposed method under such sparse control-point conditions, this section conducts an extreme stress test of the tomographic inversion constrained by a single-well prior.

In this experiment, the virtual uphole survey constraint at lateral coordinate X=3500 m was deactivated, retaining only the velocity data from the single uphole survey at X=1500 m as the prior input for the entire domain. Because the adaptive Gaussian influence radius is set to σ=500 m, the diagonal elements of the spatial weight matrix, w_i, exhibit rapid exponential decay. Specifically, in the far-field region where X>3100 m (i.e., at a distance exceeding 2σ from the wellbore), w_i drops below 0.13. Consequently, the influence of the prior constraint in this distal region is substantially diminished and becomes practically negligible.

The single-well inversion profile (Fig.3) demonstrates that within the near-wellbore region on the left, "stretching" artifacts at the lower boundary of the shallow LVZ are completely suppressed, achieving results identical to the multi-well scenario. As the inversion space extends across the transition zone toward the far-field region on the right, the natural tapering of the Gaussian weights ensures that update dominance seamlessly shifts back to the seismic traveltime data. Consequently, no numerical discontinuities, artificial pseudo-boundaries, or bulls-eye artifacts are induced across the transition interface.

Quantitative statistical analysis reveals that under the extreme single-well constraint, the global velocity RMSE increases to 8.1 m/s, up from the 5.3 m/s obtained in the uphole scenario. Despite this increase, the overall prediction error is still reduced by a substantial 47.4% compared to unconstrained conventional tomography (15.4 m/s). This sparse-data scenario strongly demonstrates the mathematical robustness of the proposed method in severely data-poor environments, confirming that the Gaussian decay mechanism inherently provides a stable and physically sound spatial transition.

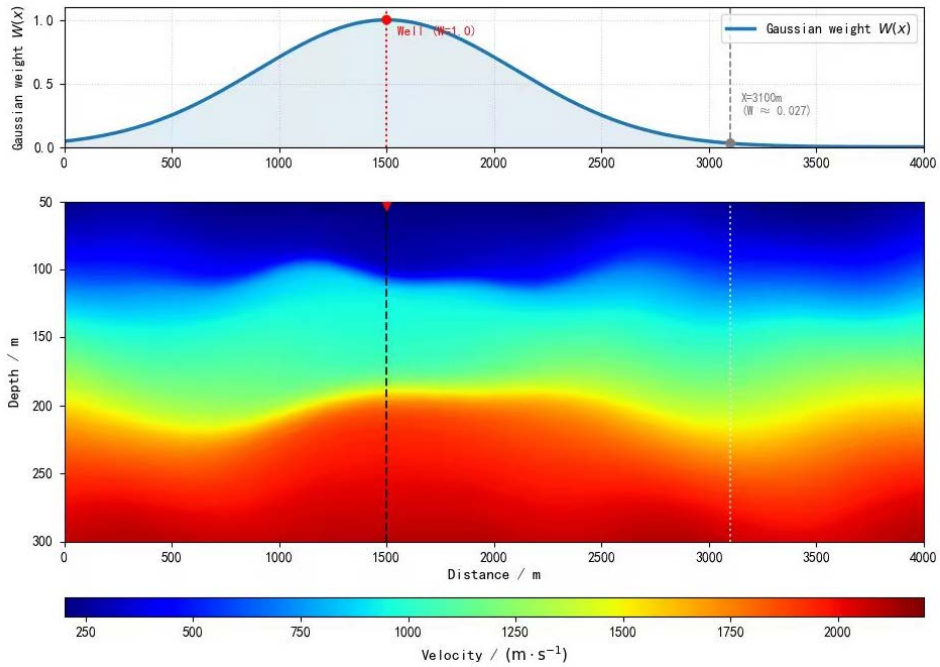


Fig.3 Inverted velocity profile under the extreme single-well constraint

Theoretical verification of the stacking RMS amplitude optimization criterion

In the preceding synthetic data tests, the optimal values for the Gaussian influence radius and the global constraint weight were determined by minimizing the global velocity RMSE. However, in actual field seismic surveys, the true subsurface velocity structure is inherently unknown (i.e., ground truth is absent), making it impossible to rely on RMSE calculations for parameter selection. To robustly and objectively apply the optimal constraint configurations derived from theoretical models to real-world datasets, this paper proposes using the maximization of the stacked RMS amplitude within a target time window as a purely data-driven evaluation criterion.

To rigorously verify the physical soundness of this evaluation criterion, a closed-loop numerical validation was conducted using the synthetic data. For the forward-modeled shot gathers, tomographic static corrections derived from a discrete range of scanned σ values were individually applied, followed by standard NMO correction and stacking procedures. Fig.4 illustrates

the coupled response curves of the true velocity RMSE and the stacked RMS amplitude within the bedrock reflection time window as a function of σ.

As clearly observed from Fig.4:

- Under-constrained Regime (Small σ): When σ is small, the spatial coverage of the prior constraint fails to adequately encompass the shallow ray shadow zones, resulting in a persistently high model RMSE. Consequently, residual long-wavelength statics severely disrupt the coherent stacking of reflection events, which ultimately degrades the stacked RMS amplitude.
- Over-smoothed Regime (Large σ): Conversely, when σ is excessively large (σ> 600 m), the true lateral velocity gradients are over-smoothed. This causes the model RMSE to rise, while the coherency of the stacked energy simultaneously degrades.
- Closed-Loop Convergence Point: Crucially, the global maximum of the stacked RMS amplitude curve aligns perfectly with the global minimum of the velocity RMSE curve, occurring at the exact same parameter value (e.g., σ= 400 m).

This independent cross-validation, conducted using a synthetic framework with a known ground truth, demonstrates that the stacked RMS energy maximization criterion holds rigorous geophysical significance. Rather than being a mere numerical artifact, it serves as a direct proxy for the fidelity of the inverted velocity model relative to the true subsurface structure. This finding establishes a solid theoretical foundation for reliably applying this criterion to complex, real-world 3D near-surface datasets.

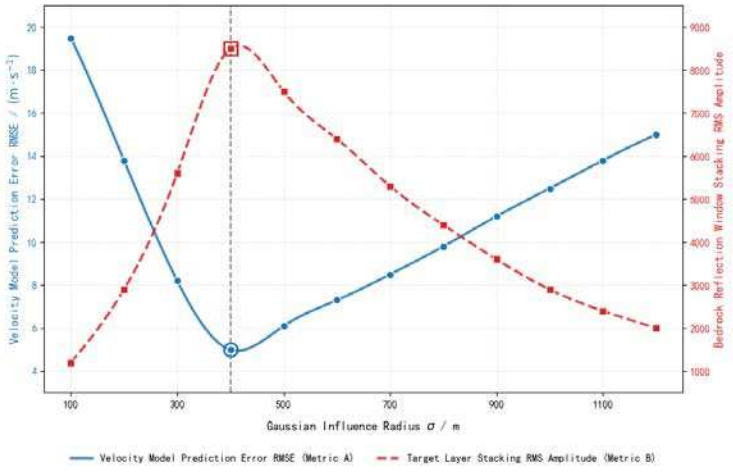


Fig.4 Coupled response curves of the true velocity RMSE and the stacked RMS amplitude versus the Gaussian influence radius σ. The dual Y-axis plot illustrates the precise closed-loop physical mapping, where the maximum stacked energy perfectly coincides with the minimum velocity inversion error (indicated by the vertical dashed line)

Real data application and parameter sensitivity

Geological background and extreme data challenges

We apply the proposed adaptively constrained tomographic inversion method to the near-surface static correction of a 3D field seismic dataset targeting the Chang 3 reservoir in the Weibei Oilfield. The study area is characterized by typical loess tableland geomorphology with dramatic topographic relief. The highly prospective Chang 3 reservoir is distinguished by an exceptionally shallow burial depth (averaging 600 m, and locally as shallow as 200 m) and thin reservoir intervals spanning only a few meters. Furthermore, the shallow low-velocity weathered layer exhibits drastic lateral thickness variations across the survey area. Compounding these geological complexities, logistical surface constraints—specifically environmentally protected zones and abandoned mined-out areas—occupy 25% of the total survey area (Fig.5). These restricted zones dictate a severely irregular seismic acquisition geometry with an extremely sparse distribution of sources and receivers. Consequently, the effective data fold for ultra-shallow formations drops strictly below 10 after NMO stretch muting.

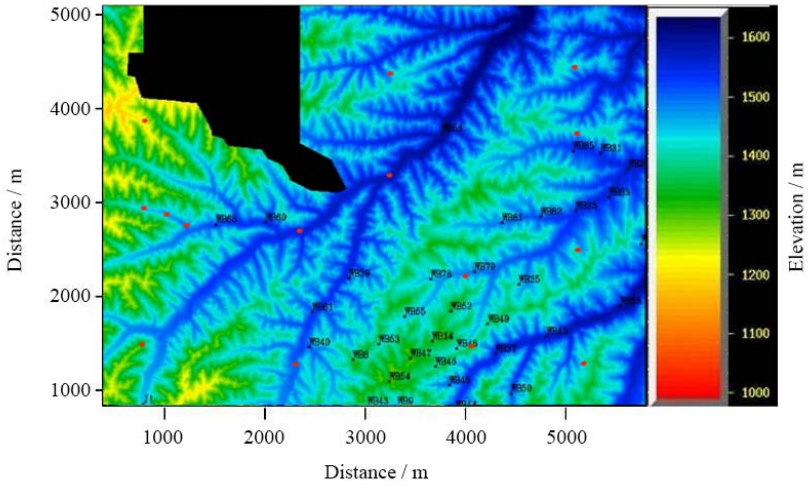


Fig.5 Acquisition geometry and surface elevation map of the real survey area in the Weibei Oilfield. Red dots denote the locations of 15 uphole survey wells with an average spacing of 1200 m. Constrained by the black shaded areas (mined-out areas, accounting for 25% of the total area), the average effective fold in the shallow 0-200 m depth range is only 5-8

In conventional processing workflows, these extreme data conditions inevitably introduce severe long- and short-wavelength static correction errors. To address this highly ill-posed modeling problem, the Gaussian influence radius σ and the global constraint weight γ serve as the core parameters governing the spatial influence of prior information and its optimal fusion proportion with the seismic observation data. Building upon the theoretical conclusions verified by the synthetic tests in Section 3.5, we adopt a fully data-driven criterion that maximizes the stacked RMS amplitude within the target formation time window. This approach ensures an accurate and objective calibration of the spatially adaptive parameters for complex field applications.

Target horizon time window extraction and high-fidelity preprocessing

To ensure the evaluated static corrections possess definitive physical significance and avoid artificial numerical enhancement,

a rigorous high-fidelity preprocessing workflow was implemented prior to objective function extraction:

(1) Amplitude-preserving compensation: Time-variant gains (e.g., AGC) were explicitly excluded. Instead, surface-consistent amplitude compensation was applied to preserve true relative reflectivities.

(2) NMO stretch muting: A strict 30% stretch limit was enforced to eliminate distorted, low-frequency far-offset signals and prevent stretch-induced inversion artifacts.

(3) Adaptive horizon-guided window: Guided by precise well ties at Key Well No. 1, an 80-ms spatially adaptive window (40 ms) was constructed around the basal boundary of the Chang 3 reservoir. Within this window, the stacked RMS amplitude serves as the quantitative objective function for calibrating the spatial constraint parameters:

$$\mathrm{RMS} = \sqrt{\frac{1}{N}\sum_{i=1}^{N} x_i^2} \tag{9}$$

where x_i denotes the amplitude of the i-th sample point within the time window tracked along the Chang 3 reservoir horizon, and N represents the total number of samples in this evaluation window.

Crucially, optimizing solely for RMS amplitude risks introducing local artifacts via cycle skipping, which artificially aligns traces at the expense of high-frequency resolution. To mitigate this, the workflow monitors the dominant frequency and spectral bandwidth in real-time, ensuring the energy increase strictly stems from broadband, in-phase physical stacking.

Fig.6 compares the inverted velocity profiles derived from the two tomographic strategies. As shown in Fig.6(a), conventional smoothing tomography is severely hampered by the aforementioned shallow ray shadow zones. Consequently, the inverted model fails to accurately characterize the shallow LVZs and velocity inversions, resulting in a pronounced overestimation of near-surface velocities. Specifically, the conventional model yields surficial LVZ velocities of 700-800 m/s, whereas the true velocities are strictly 300-500 m/s, highlighting a substantial margin of error.

In stark contrast, the proposed adaptive constrained tomography (Fig.6(b)) leverages prior uphole survey data to significantly improve the delineation of the highly variable LVZ bottom boundary. The constrained velocity model successfully corrects and stabilizes the LVZ velocity within the true physical range of 300-500 m/s. Furthermore, the shallow model exhibits superior numerical stability alongside natural spatial smoothness. The high-frequency spatial resolution within the LVZ is substantially enhanced, yielding a much more refined and precise characterization of the stratigraphic interfaces.

This comparative analysis conclusively demonstrates that, during the first-arrival tomography of sparse-shot data, the uphole survey constraint mechanism effectively compensates for the inherent lack of near-offset information in long-spread geometries. Consequently, it enables the construction of a high-precision near-surface velocity model of the loess tableland that strictly adheres to geological principles. This, in turn, provides a robust data foundation for resolving severe static correction challenges and accurately evaluating seismic source performance.

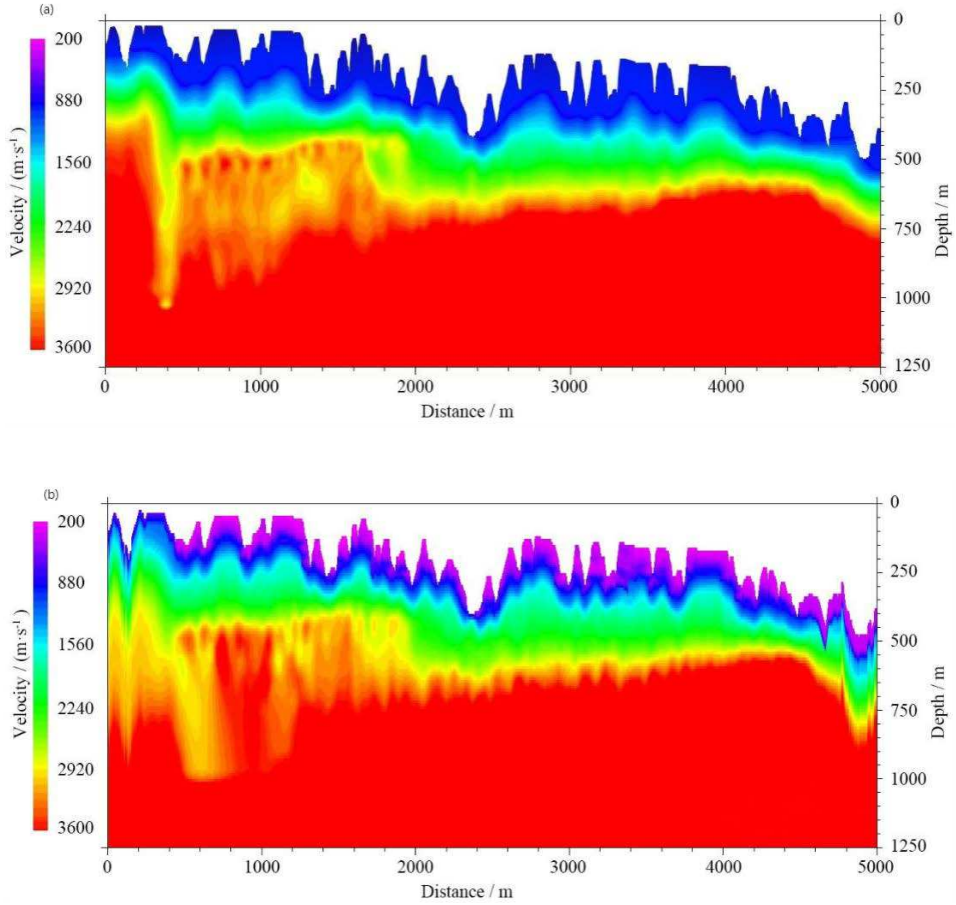


Fig.6 Inverted velocity model obtained by conventional tomographic static correction (a) and constrained tomographic static correction(b)

Furthermore, the practical efficacy of these corrections is demonstrated in both shot gathers (Fig.7) and stacked sections (Fig.8). Prior to correction (Fig.7(a)), severe near-surface heterogeneity distorts first arrivals and obscures reflection events within a high-noise background. Following the adaptive constrained tomographic correction (Fig.7(b)), first arrivals recover smooth, well-aligned kinematic signatures, while reflection events exhibit distinct hyperbolic moveouts consistent with theoretical expectations. Fig.8 compares stacked sections processed using different static correction methods. Fig.8(a) presents the result obtained from conventional tomographic static correction. In contrast, the proposed constrained tomographic static correction (Fig.8(b)) yields superior reflector continuity and clearer reflection wave packages. These results validate the robustness of the proposed framework under extreme field conditions, which is primarily attributed to the more accurate near-surface velocity model reconstructed by the constrained tomographic inversion.

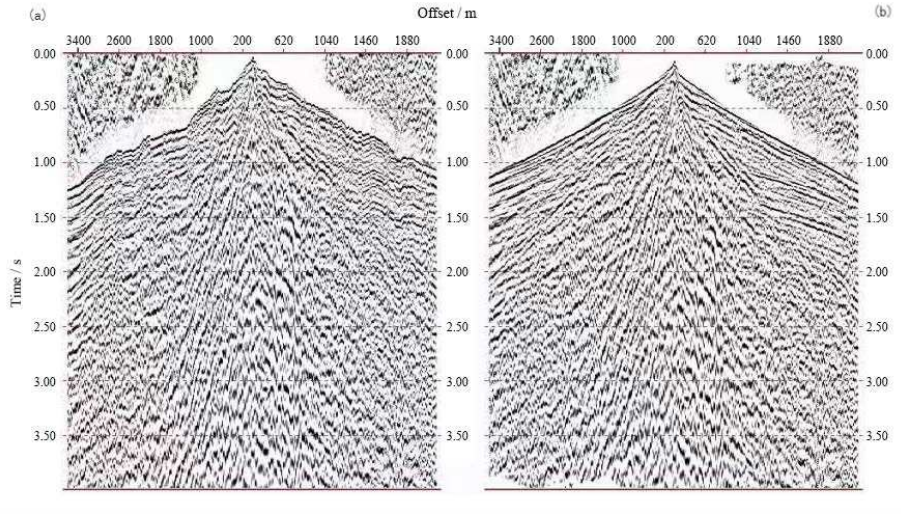


Fig.7 Comparison of a single-shot gather before(a) and after(b) the adaptive constrained tomography split-wavelength static corrections

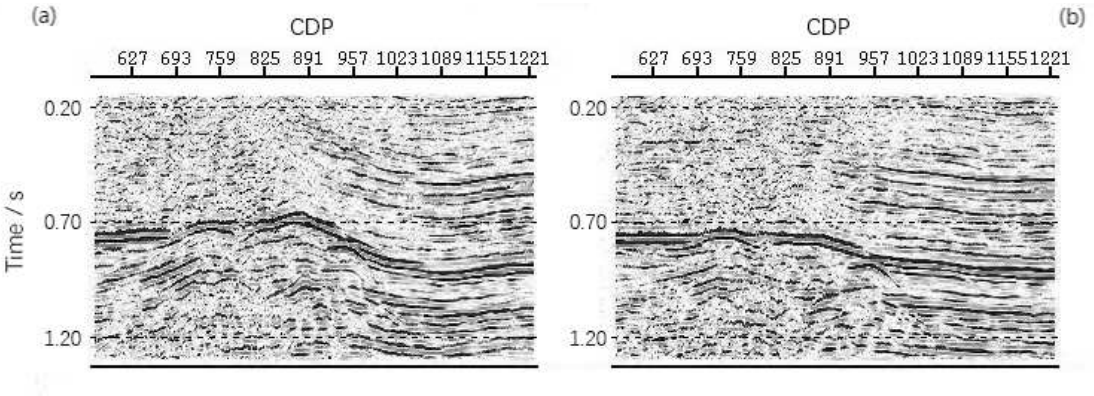


Fig.8 Comparison of stack section by conventional tomographic static correction (a) and constrained tomographic static correction(b)

Independent validation via blind wells and sensitivity analysis

Optimizing the Gaussian radius σ solely on stacked RMS amplitude risks "circular reasoning," as maximum amplitude does not guarantee a physically accurate velocity model. To circumvent the risk of circular reasoning, we adopted an independent blind-well validation strategy. Well No. 3, situated in a zone of abrupt reflection energy transitions and the strongest near-surface lateral heterogeneity in the survey area, was selected as the most stringent verification point and intentionally withheld from the prior constraint dataset. Analyzing the coupled response of the survey-wide stacked RMS amplitude and the blind-well velocity prediction error ($RMSE_{blind}$) reveals a clear trend: when the stacked amplitude reaches its global maximum at σ= 500 m, $RMSE_{blind}$ perfectly coincides with its global minimum of 12 m/s.

This convergence illustrates the core physical mechanism of the adaptive constraint strategy. Under extremely low-fold conditions, purely data-driven global smoothing suffers from sparse ray paths, causing local spatial singularities in the Jacobian matrix and inducing severe near-surface velocity distortions. In contrast, the optimal radius (σ=500 m) naturally envelops the blind well within the prior-information transition zone of adjacent uphole survey. This Gaussian weighting establishes a reliable low-frequency background velocity field, upon which even sparse ray coverage provides sufficient residual constraints to resolve high-frequency details, effectively overcoming nonlinear local minima.

Further sensitivity tests—including varying time-window dimensions (±20 ms to ±100 ms) and random common midpoint (CMP) subset sampling (30% and 60% of total volume)—confirm that the global maximum of the RMS energy curve remains robustly anchored at σ=500 m, demonstrating high resilience against field data uncertainties.

To provide final physical validation, Fig.9 presents stacked sections and co-registered near-surface velocity models under three parameter scenarios:

(1) Weak constraint (σ=200 m, Fig.9(a)): The spatial influence of prior information decays too rapidly. The velocity profile exhibits chaotic, short-wavelength numerical anomalies in inter-well regions, causing severe kinematic distortions and artificial pseudo-faults in the mid-to-deep reflections.

(2) Optimally parameterized (σ=500 m, Fig.9(b)): The velocity profile sharply reconstructs the heterogeneous low-velocity layer and the bedrock boundary. The Chang 3 reservoir horizon achieves peak RMS amplitude, and its structural geometry exhibits strong spatial consistency with the velocity model's geological architecture.

(3) Over-smoothed scenario (σ=2000 m, Fig.9(c)): The excessively large influence radius causes the prior spatial interpolation to dominate the updates, failing to resolve high-frequency near-surface variations. While reflection events maintain apparent continuity, genuine micro-structures and small-scale fault offsets are artificially smeared and obscured.

Ultimately, this independent, physically grounded cross-validation definitively proves that the stacked energy peak is not a mathematical coincidence, but rather the direct physical manifestation of an optimally reconstructed subsurface velocity model.

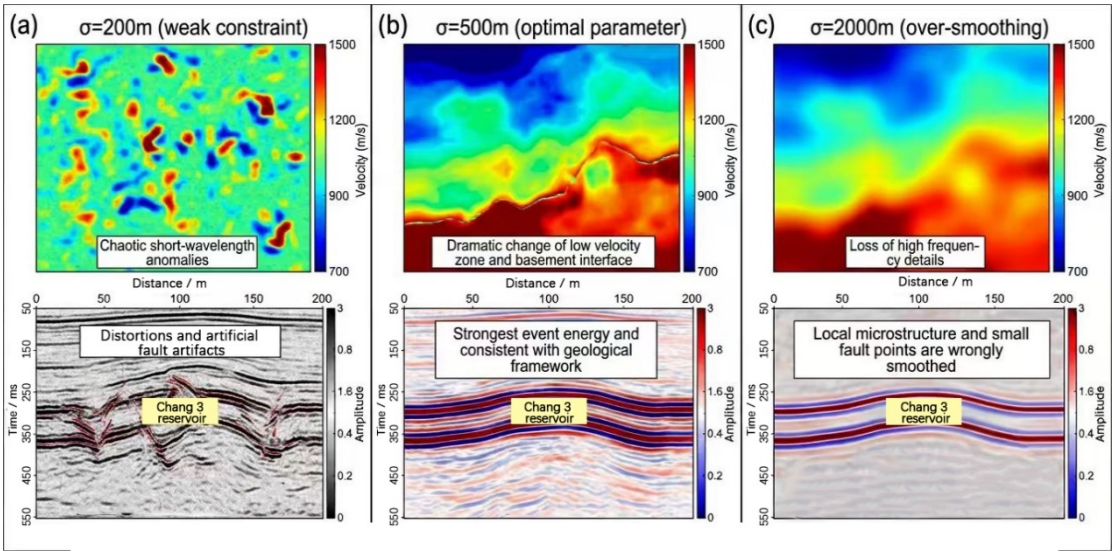


Fig.9 Comparative panels of the field data from the Weibei survey area under different offline parameter-scanning scenarios of σ. In panels (a)-(c), the upper sections display the inverted near-surface velocity model slices, while the lower sections present the corresponding stacked seismic sections within the target time window of the Chang 3 reservoir: (a) σ=200 m, (b) σ=500 m, and (c) σ=2000 m

Parameter matching mechanism among uphole survey density, near-surface heterogeneity scale, and gaussian radius

To explicitly define the applicability limits of the proposed method and prevent introducing erroneous prior constraints into inter-well regions, let L_{well} denote the average uphole survey spacing across the survey area and L_{hetero} represent the characteristic spatial scale of near-surface lateral heterogeneity. In scenarios characterized by strong heterogeneity and sparse well coverage ($L_{well} \gg L_{hetero}$), selecting the adaptive Gaussian radius σ requires adhering to a strict upper bound:

$$\sigma \leq \frac{L_{well}}{2} \text{ and } \sigma \leq L_{hetero} \tag{10}$$

Theoretical derivations demonstrate that when the spatial distance d_i between an inversion grid node and an uphole survey exceeds 2σ, the Gaussian weighting function decays exponentially to a physically negligible state. However, a rigorous quantitative re-evaluation of this physical mechanism is required when contextualized by the specific parameter configuration of our study area (σ=500 m, L_{well}=1200 m).

In this field survey, the maximum theoretical distance from any unconstrained grid node to the nearest uphole survey is $d_{max}=L_{well}/2$=600 m. Based on the spatial decay of the Gaussian kernel, the prior constraint weight at the midpoint between wells evaluates to approximately 0.486. This result confirms our theoretical design: under the optimal influence radius of (σ=500 m), the Gaussian influence fields from adjacent control wells overlap significantly within inter-well zones. Here, the effective influence width of 2σ=1000 m spans the 1200 m well spacing effectively, constructing a background "soft constraint" field with a minimum weight of 0.486.

In challenging scenarios characterized by ultra-low fold or expansive ray-path blind zones, purely data-driven traveltime updates and conventional mathematical smoothing are insufficient for stable inversion. Under these critical conditions, this overlapping soft constraint provides the essential physical prior support needed to effectively regularize the null space caused by ray sparsity.

Ultimately, rather than requiring a high spatial density of uphole survey, the proposed method dynamically aligns the Gaussian radius σ with both the actual well spacing and the characteristic scale of geological heterogeneity. This parameter matching achieves a physically smooth and numerically stable transition between local, near-well strong constraints and inter-well soft constraints.

Quasi-decoupling analysis of constraint weights and gaussian radius via robustness cross-validation

Although absolute decoupling between the global weight parameter and the Gaussian radius σ cannot be achieved analytically within the highly nonlinear tomographic objective function, experimental results demonstrate that Equation (6) successfully transforms their inherently strong parametric coupling into a fault-tolerant, weakly cross-dependent structure. By leveraging this trace-normalized alternating optimization strategy, the proposed framework achieves strong parametric robustness.

This "quasi-decoupling" mechanism fundamentally circumvents the canyon effects and local minima that frequently plague joint optimization within the two-dimensional parameter space (α, σ). Consequently, dimension-reduced single-parameter scanning based on the L-curve principle becomes highly reliable. This reduces the computational cost of determining optimal regularization parameters by an order of magnitude, establishing a robust algorithmic foundation for processing large-scale 3D field datasets.

Cross-parameter sensitivity experiments corroborate this stability. When the global dimensionless total energy coefficient is perturbed across a broad range, from 0.75 (weak constraint) to 3.00 (strong constraint), the maxima of the RMS response

convergence curves consistently anchor near σ=500 m across varying energy backgrounds.

Geophysically, the parameter γ (controlled by α) dictates the total energy of the prior constraints applied to the inversion system, while σ determines the spatial decay of this constraint across the model domain. Provided the global constraint energy remains within the well-conditioned regime delineated by the L-curve, the optimal spatial transition radius σ becomes independent of the global weight magnitude. Instead, it is governed by the true spatial correlation length of near-surface heterogeneity (i.e., the long-wavelength statics scale), achieving a genuine mathematical decoupling of spatial scale and absolute weight.

Ultimately, these rigorous tests demonstrate that the proposed adaptive parameter optimization scheme achieves a high degree of parameter independence at a practical engineering level. This grants the method exceptional stability against complex geological challenges and highlights its significant potential for industrial-scale deployment.

Discussion

Extension and future perspective of anisotropic constraints under complex surface conditions

Complex near-surface environments, such as loess tablelands, frequently exhibit strong azimuthal anisotropy in three-dimensional space. Their shallow velocity architectures are profoundly controlled by depositional strikes or the spatial distribution of paleo-gullies. In this study, Equation (3) constructs a simplified anisotropic weighted spatial distance by independently decoupling the horizontal and vertical Gaussian decay radii. However, while this formulates a functional axis-aligned Gaussian ellipsoidal weight model, it remains insufficient to fully characterize actual geological structures that extend along arbitrary azimuths.

In future research, we plan to replace the current Euclidean distance variants with the Mahalanobis distance based on a full covariance matrix. This will allow us to construct an a priori Gaussian ellipsoidal weight model capable of arbitrary rotation within the 3D space. For practical engineering implementation, we will employ a purely data-driven strategy to quantitatively extract and construct this full covariance matrix. This can be achieved by utilizing either the spatial distribution characteristics of uphole survey clusters within the survey area or geostatistical variograms derived from high-fidelity seismic attributes. Ultimately, this initiative will achieve a seamless match between the prior information's constraint footprint and the true geological structural strike, significantly enhancing the inversion fidelity of complex near-surface tomography.

Computational cost analysis and generalizability

In large-scale 3D inversions for actual production, computational cost serves as a critical metric for evaluating an algorithm's industrial viability. Theoretical analysis reveals that the proposed method imposes no additional intervention on the massive and computationally expensive Jacobian matrix $\mathbf{G}$. Instead, it merely injects a highly sparse diagonal matrix, $\gamma\mathbf{W}^{\mathbf{T}}\mathbf{W}$, into the system during the construction of the regularization matrix. This streamlined algorithmic design effectively circumvents the evaluation of complex non-linear cross-terms, ensuring that the increases in both computation time and memory consumption per iteration are theoretically estimated to be less than 2% compared to conventional smoothing tomography.

Synthesizing theoretical analyses and field inversion results reveals that the essential mechanism of the adaptive Gaussian prior constraint is not to globally eliminate the singularity of the Hessian matrix. Rather, it operates by injecting high-confidence physical gradients around known control points, thereby precisely repairing the severe ill-conditioning of the local Hessian matrix caused by extreme ray scarcity in the shallow near-surface. However, in far-field blind zones distant from uphole survey control, the global numerical convergence of the normal equations continues to rely on the synergistic

regularization provided by the global smoothing operator.

The core algorithmic advantage of the proposed framework lies in forging a profound physical coupling between the two regularization mechanisms. The local Gaussian prior weights serve as robust, absolute physical "anchors" that rigorously constrain the null space of the global solution. This successfully circumvents the non-linear inversion traps that frequently induce severe velocity stretching artifacts in the extremely shallow near-surface. Concurrently, the global smoothing operator ceases to act as a passive soft constraint that indiscriminately blurs high-frequency details. Instead, it transitions into a physical spatial evolution operator that securely and smoothly propagates the localized stability of the uphole data outward, guaranteeing the numerically safe convergence of the model across expansive, weakly constrained far-field regions. This dynamic interplay between localized absolute strong constraints and global relative smooth evolution fundamentally mitigates the severe non-uniqueness triggered by ultra-low effective fold in irregular loess tableland surveys. Consequently, the finalized inversion system is not only mathematically well-conditioned but also demonstrates exceptional physical plausibility.

Regarding geological generalizability, the fundamental premise underpinning this method is utilizing sparse, absolute physical measurements to robustly anchor ray-path blind zones plagued by ultra-low fold. This core physical logic is not exclusively applicable to loess tablelands; rather, it is highly adaptable to a myriad of other complex near-surface scenarios facing similar data-deficiency challenges, such as:

- Desert dune environments: Regions exhibiting massive velocity contrasts and dramatic lateral variations between thick, unconsolidated sand dunes and the underlying high-velocity mudstone basement;
- Piedmont moraines and thick gravel layers: Scenarios devoid of high signal-to-noise ratio (SNR) traveltimes, where pervasive strong scatterers severely attenuate ultra-shallow first-arrival energy, rendering accurate first-break picking nearly impossible.

Ultimately, provided the target survey area can supply representative uphole survey data to establish a spatial a priori framework, the proposed approach serves as a highly versatile, computationally efficient, and high-precision solution for complex statics corrections.

Limitations of the optimization strategy

The control-variable-based "two-step alternating optimization" strategy adopted in this study is intrinsically a dimensionality-reduction approximate search scheme. Within the highly ill-posed objective function space of traveltime inversion, a profound non-linear coupling inevitably exists between the total energy of the constraint strength (controlled by α) and its spatial footprint (dictated by σ).

Particularly when realistic geological heterogeneity is exceptionally strong, deriving α_{opt} while artificially freezing the initial Gaussian radius σ_0 at a constant empirical value is highly likely to fail in yielding the absolute global optimum within the joint parameter space, strictly in a numerical and topological sense. Consequently, the system carries a theoretical risk of converging to local minima. Nevertheless, for industrial-scale 3D production processing, the computational overhead required to execute an exhaustive grid search across high-dimensional hyperparameter spaces is entirely prohibitive.

Conclusion

To address the challenges of high-fidelity near-surface imaging and statics corrections under the dual constraints of complex topography and ultra-low effective fold, this paper proposes an adaptive constrained first-arrival tomography method driven by Gaussian-decaying prior information from uphole survey. The primary conclusions of this study are summarized as follows:

(1) Mathematical reconstruction of the objective function and null-space elimination: By embedding absolute slowness data as prior regularization constraints into the tomographic objective function, we construct a Gaussian weighting matrix that decays exponentially with spatial distance. Mathematically, this mechanism overcomes the severe singularity of the Jacobian matrix, a flaw inherently caused by the scarcity of intersecting rays in the ultra-shallow subsurface during conventional tomography. Consequently, it drastically suppresses the velocity stretching and bulls-eye artifacts induced by inversion non-uniqueness.

(2) Theoretical validation of imaging fidelity within extreme ray-path blind zones: Using a synthetic model characterized by dramatic thickness variations in the loess layer and severe topographic relief, we quantitatively demonstrate that the proposed method significantly reduces the RMSE of the inverted velocity model. Even within data blind zones plagued by extremely low effective ray-hit rates, the method achieves precise, high-fidelity reconstruction of both the undulating basal morphology of the LVZ and concealed, deep-seated high-velocity anomalies.

(3) Data-driven parameter optimization closed-loop: We propose and rigorously justify a quantitative evaluation criterion based on maximizing the stacked RMS amplitude within the target horizon time window. Validated via blind-well testing, this criterion transforms parameter tuning from a subjective, empirically reliant process into an objective, fully reproducible closed-loop system. Without incurring additional field acquisition costs, this research unlocks the latent imaging potential of historical restricted-geometry datasets, providing a highly adaptable framework for the high-precision imaging of shallow, thin interbedded strata.

Acknowledgements

This research was jointly supported by the National Natural Science Foundation of China (42504128), the Project of Science and Technology Department of Henan Province (242300421461), and the Project of Earthquake Administration of Henan Province (2024182). Herein, we would like to express our sincere gratitude to all the funding units, and thank the reviewers for their insight reviews and comments which helped to improve this article.

Author contributions

Huo Yuanyuan performed the data analysis, implemented the algorithms, and developed the models. Yang Rui supervised the research and contributed to the manuscript writing. Qi Hui contributed to the manuscript editing. Li Xin performed the data collection and analysis. All authors reviewed and approved the final version of the manuscript.

Data availability Statement

The data that support the findings of this study are not openly available due to reasons of sensitivity and are available from the corresponding author upon reasonable request.

Declarations

Conflict of interest: The authors declared that they have no competing interest or any commercial or associative interest in connection with the work submitted.

Reference

[1]. Bakulin A, Woodward M, Nichols D et al (2009) Localized anisotropic tomography with well information in VTI media. Geophysics 75(5):37–45. https://doi.org/10.1190/1.3481702

[2]. Bregman ND, Bailey RC, Chapman CH (1989) Ghosts in tomography: the effects of poor angular coverage in 2-D seismic traveltime inversion. Can J Explor Geophys 25(1):7–27

[3]. Bube KP, Meadows MA (1999) The null space of a generally anisotropic medium in linearized surface reflection tomography. Geophys J Int 139(1):9–50. https://doi.org/10.1046/j.1365-246x.1999.00910.x

[4]. Chang X, Liu Y, Wang H et al (2002) 3-D tomographic static correction. Geophysics 67(4):1275–1285. https://doi.org/10.1190/1.1500390

[5]. Charles S, Mitchell D, Holt R et al (2008) Data-driven tomographic velocity analysis in tilted transversely isotropic media: A 3D case history from the Canadian Foothills, Geophysics 73(5):261–268. https://doi.org/10.1190/1.2952915

[6]. Dahl-Jensen T (1989) Static corrections on crystalline rocks. Geophys Prospect 37(5):467–478. https://doi.org/10.1111/j.1365-2478.1989.tb02218.x

[7]. Dai HT, Cheng JB, Wang HB et al (2020) A shallow velocity modeling technique for complex surfaces. Geophys Prospect Pet 59(3):336-343. https://doi.org/10.3969/j.issn.1000-1441.2020.03.002

[8]. Goudswaard J, ten Kroode F, Snieder R et al (1998) Detection of lateral velocity contrasts by crosswell traveltime tomography. Geophysics 63(2):523–533. https://doi.org/10.1190/1.1444352

[9]. Grote MJ, Kray M, Nahum U (2017) Adaptive eigenspace method for inverse scattering problems in the frequency domain. Inverse Probl 33(2):025006. https://doi.org/10.1088/1361-6420/aa5250

[10]. Hestenes MR, Stiefel E (1952) Methods of conjugate gradients for solving linear systems. J Res Natl Bur Stand 49(6):409–436. https://doi.org/10.6028/jres.049.044

[11]. Hu ZD, He ZH, Wang XW et al (2010) Application of non ray-tracing tomography static correction technique in Loess Plateau. Oil Geophys Prospect 45:94–100. https://doi.org/j.cnki.issn.1000-7210.2010.s1.050

[12]. Huo YY, Yang R, Pan JS et al (2024) A 3D surface wave attenuation method based on dispersion curve analysis and its application. Acta Geophysica 72(6):4123-4138. https://doi.org/10.1007/s11600-024-01318-2

[13]. Ivansson S (1986) Seismic borehole tomography—theory and computational methods. Proc IEEE 74(2):328–338. https://doi.org/10.1109/PROC.1986.13459

[14]. Jin S, Madariaga R, Virieux J et al (1992) Two-dimensional asymptotic iterative elastic inversion. Geophys J Int 108(2):575–588. https://doi.org/10.1111/j.1365-246X.1992.tb04637.x

[15]. Jordi C, Doetsch J, Günther T et al (2018) Geostatistical regularization operators for geophysical inverse problems on irregular meshes. Geophys J Int 213(2):1374–1386. https://doi.org/10.1093/gji/ggy055

[16]. Ju XG, Yu QL (2017) Research and application of the long wavelength static correction technology with well control in the loess plateau area. Prog Geophys 32(3):1149-1153. https://doi.org/10.6038/pg20170326

[17]. Li P, Feng Z, Li Z et al (2004) Static correction technology and applications in complex areas of western China. SEG Tech Program Expand Abstr:1441–1444. https://doi.org/10.1190/1.1839669

[18]. Li S, Zhang X, Dan Z et al (2021) Geological guided tomography inversion based on fault constraint and its application. J Ocean Univ China 20(6):1419–1430. https://doi.org/10.1007/s11802-021-4667-6

[19]. Linari V (2004) A practical approach to well-seismic data calibration. Lead Edge 23(8):774–775. https://doi.org/10.1190/1.1786900

[20]. Liu ZK, Wu YG, Liu YJ et al (1995) Near-surface static correction method using first-arrival traveltimes velocity tomography. Chin J Geophys 38(S1):153–159

[21]. Morozov IB (2004) Null-space and statistical significance of first-arrival traveltime inversion. Geophys J Int 156(3):549–554. https://doi.org/10.1111/j.1365-246X.2004.02133.x

[22]. Nocedal J, Wright SJ (2006) Numerical optimization. Springer, New York. https://doi.org/10.1007/978-0-387-40065-5
[23]. Portniaguine O, Zhdanov MS (1999) Focusing geophysical inversion images. Geophysics 64(3):874–887. https://doi.org/10.1190/1.1444596
[24]. Pratt RG, Chapman CH (1992) Traveltime tomography in anisotropic media—II. Application. Geophys J Int 109(1):20–37. https://doi.org/10.1111/j.1365-246X.1992.tb00076.x
[25]. Rao Y (2007) Seismic tomography for velocity and attenuation model reconstruction. Dissertation, Imperial College London. http://hdl.handle.net/10044/1/11882
[26]. Rawlinson N, Sambridge M (2005) The fast marching method: an effective tool for tomographic imaging and tracking multiple phases in complex layered media. Explor Geophys 36(4):341–350. https://doi.org/10.1071/EG05341
[27]. Ronen J, Claerbout JF (1985) Surface-consistent residual statics estimation by stack-power maximization. Geophysics 50(12):2759–2767. https://doi.org/10.1190/1.1441896
[28]. Shepard D (1968) A two-dimensional interpolation function for irregularly-spaced data. Proc 1968 23rd ACM Natl Conf:517-524. https://doi.org/10.1145/800186.810616
[29]. Simmons NA, Myers SC, Johannesson G et al (2012) LLNL-G3Dv3: global P-wave tomography model for improved regional and teleseismic travel time prediction. J Geophys Res Solid Earth 117(B10):B10302. https://doi.org/10.1029/2012JB009525
[30]. Soni A, Plessix R, Huiskes M (2019) A comparison of ray-based traveltime and waveform inversion results for depth velocity model building in complex fold and thrust belts. Geophysics 84(6): R1019–R1031. https://doi.org/10.1190/geo2019-0082.1
[31]. Tikhonov AN, Arsenin VY (1978) Solutions of ill-posed problems. Mathematics of Computation 32(144): 1320-1322. https://doi.org/10.2307/2006360
[32]. Trinks I, Singh SC, Chapman CH et al (2005) Adaptive traveltime tomography of densely sampled seismic data. Geophys J Int 160(3):925–938. https://doi.org/10.1111/j.1365-246X.2005.02531.x
[33]. Xiao YX, Yang HS, Cui ST et al (2019) An efficient refraction static method for massive seismic data. Oil Geophys Prospect 54(4):768-774. https://doi.org/10.13810/j.cnki.issn.1000-7210.2019.04.006
[34]. Yu YY, Cao DY, Xing CY et al (2016) Application of the technology of model constraint refraction statics on loess area. Prog Geophys 31(3):1373-1380. https://doi.org/10.6038/pg20160361
[35]. Zhang L, Wang Y (2024) First-arrival traveltime tomography with near-surface structural segularization. IEEE Trans Geosci Remote Sens 62:1–14. https://doi.org/10.1109/TGRS.2024.3434396
[36]. Zhu X, Zhao R, Gray S et al (2024) Seismic imaging in Tarim Basin: Overcoming complex near-surface conditions. AAPG Annu Conv Exhib:2489-2493. https://doi.org/10.1190/image2024-4087690.1